ACS APPLIED MATERIALS & INTERFACES

Research Article

Cite This: ACS Appl. Mater. Interfaces 2018, 10, 33457−33463

www.acsami.org

# High-Vacuum Particulate-Free Deposition of Wafer-Scale Mono-, Bi-, and Trilayer Molybdenum Disulfide with Superior Transport Properties

Kortney Almeida, Michelle Wurch, Adane Geremew, Koichi Yamaguchi, Thomas A. Empante, Michael D. Valentin, Michael Gomez, Adam J. Berges, Gordon Stecklein, Sergey Rumyantsev,[†] Joseph Martinez, Alexander A. Balandin, and Ludwig Bartels*

Materials Science & Engineering Program, University of California at Riverside, Riverside, California 92521, United States

Supporting Information

**ABSTRACT:** Wafer-scale $MoS_2$ growth at arbitrary integer layer number is demonstrated by a technique based on the decomposition of carbon disulfide on a hot molybdenum filament, which yields volatile $MoS_x$ precursors that precipitate onto a heated wafer substrate. Colorimetric control of the growth process allows precise targeting of any integer layer number. The method is inherently free of particulate contamination, uses inexpensive reactants without the pyrophoricity common to metal−organic precursors, and does not rely on particular gas-flow profiles. Raman mapping and photoluminescence mapping, as well as imaging by electron microscopy, confirm the layer homogeneity and crystalline quality of the resultant material. Electrical characterization revealed microampere output current, outstanding device-to-device consistency, and exceptionally low noise level unparalleled even by the exfoliated material, while other transport properties are obscured by high-resistance contacts typical to $MoS_2$ devices.

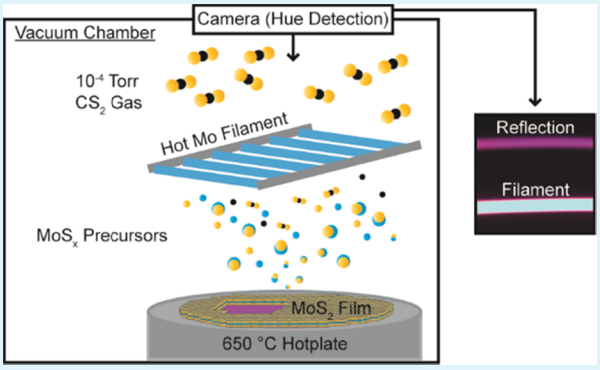


**KEYWORDS:** *chemical vapor deposition, transition metal dichalcogenides, wafer-scale growth, transport noise measurements, colorimetry*

## INTRODUCTION

Mono- and few-layer transition metal dichalcogenide (TMD) films, particularly $MoS_2$ and $WSe_2$, are promising candidate materials in the continuing miniaturization of semiconductor devices. They combine a robust well-defined semiconducting behavior with appreciable processing stability.[1−3] Indeed, it has been shown that at the monolayer limit, they offer unparalleled on−off ratio,[4] subthermionic tunnel field-effect transistor (FET) performance,[5] and unique electronic and optical properties.[6−9] The wide band-gap of few-layer $MoS_2$ makes it promising for high-temperature applications.[10] It has also been demonstrated that $MoS_2$ is a versatile sensor material.[11,12] While semiconductor devices conventionally utilize the substrate semiconducting material as the transistor channel, introduction of vertical cell access transistors called for by the International Technology Roadmap for Semiconductors in 2019 requires the deposition of high-quality channel materials after initial patterning steps. Here, two-dimensional (2D) van der Waals (vdW) materials offer the advantage of very shallow channels at reduced surface scattering. Previous methods to produce wafer-scale monolayer TMD films have included tube-furnace chemical vapor deposition (CVD),[13−19] liquid-phase exfoliation,[20−22] and metal−organic CVD or atomic layer deposition.[23−30] These techniques utilize chloride, sulfide, or oxide-based transition metal precursor powders or high-vapor-pressure carbonyls/metal−organic compounds. An ideal deposition method produces high-quality homogeneous films at arbitrary integer layer number and wafer-scale coverage without the use of any powder or pyrophoric precursor to avoid particulate contamination and processing hazards. Here, we show the growth of wafer-scale continuous $MoS_2$ films by a process that fulfills all of these requirements and yields a material superior in current noise characteristics to exfoliated and powder CVD films.

Our process departs significantly from the prior work by the use of a set of metallic molybdenum filament wires (Alfa Aesar) as the molybdenum source. Figure 1a shows a schematic of our growth setup. The method utilizes the difference in volatility between molybdenum metal (melting point: 2623 °C) and $MoS_2$ (melting point: 1185 °C) as well as other $MoS_x$ species; this ensures that exclusively $MoS_x$ species are released from the filaments. Consequently, the material

Received: June 29, 2018
Accepted: September 7, 2018
Published: September 7, 2018






DOI: 10.1021/acsami.8b10857
ACS Appl. Mater. Interfaces 2018, 10, 33457−33463

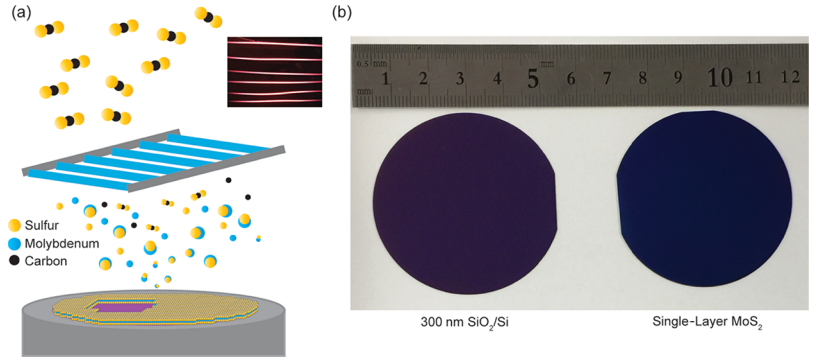


**Figure 1.** (a) Schematic of the high-vacuum growth process utilizing a set of directly heated molybdenum filaments and carbon disulfide as the chalcogen source. Volatile $MoS_x$ precursors are formed at the filament and precipitate onto the heated substrate coalescing into a continuous and crystalline film. Inset: photograph of heated filaments; (b) photograph of substrates before and after single-layer $MoS_2$ growth.

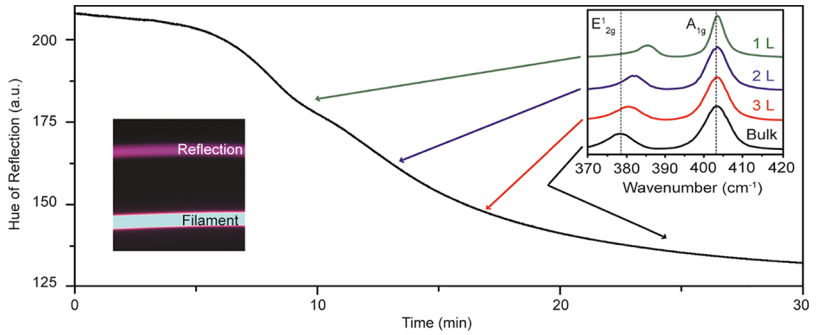


**Figure 2.** Hue (0−255) of the Mo-rod reflection (top in the left inset) during film deposition. The hue curve reveals the completion of layers, for which Raman spectra are shown in the right inset.

deposited onto the substrate is already of the correct elemental composition and sufficiently surface-mobile to arrange itself into large grains and, ultimately, a continuous film. A background of carbon disulfide gas at a pressure of $6 \times 10^{-4}$ Torr (compared to a base pressure of the reactor of $1 \times 10^{-7}$ Torr) is used as a sulfur source for the formation of $MoS_x$ species on the filaments and to assure the stoichiometry in the resultant film. At a process time of up to 60 min depending on the layer number, a continuous and homogeneous single-layer film of $MoS_2$ is deposited at the wafer scale (Figure 1b).

A number of prior studies[31−33] have addressed the CVD growth of $MoS_2$ single layers and found a sequence of nucleation and in-plane aggregation. Figure 2a illustrates how we control the film growth: light from the hot molybdenum filaments (inset in Figure 1a) is reflected from the wafer substrate during growth. As $CS_2$ molecules decompose at the molybdenum filaments, $MoS_x$ precursors evolve, evaporate from the rods, and deposit onto the substrate where they obtain stoichiometric sulfur contents from the environmental $CS_2$ and form into extended islands—or evaporate again, given the high platen temperature of 650 °C. In a balance between incoming $MoS_x$ species and evaporation of the material, the film ripens into larger and larger crystalline islands. The growth rate is highest when a sizable number of large grains have formed that are stable from evaporation and offer edge sites for growth; it is lowest whenever a layer is complete.

In this work, we employ concomitant measurement of the hue of the specular-reflected Mo-filament light from the substrate for process control. This approach is novel for process control, but the dependence of the substrate color on single- and few-layer films has been well understood. Blake et al. described the contrast and color dependence of graphene on different thickness $SiO_2$ layers on Si using a multiple internal reflection method.[34] This description has since been expanded, for instance by Zhang et al.,[35] to reveal wavelength-/color-dependent amplification in $MoS_2$ imaging and spectroscopy.

## RESULTS AND DISCUSSION

Figure 2 shows the hue value of the light from the molybdenum filament reflected on the substrate as the film is growing layer by layer. The hue value is obtained by pointing a video camera from above and through the gaps of the glowing molybdenum rods at the sample during growth. Translation of the camera's red-green-blue-encoded signal into the common hue−saturation−brightness format yields the hue value, which cycles through the color circle from 0 to 255. The inset in Figure 2a shows the camera view on the filament in the bottom and its reflection from the substrate in the top. Numeric color temperature correction based on the albedo of the filament (bottom) has the power of removing dependence of the hue signal of the reflection (top) from the filament temperature but is not commonly required for the growth.

The main graph of Figure 2 shows the evolution of the hue value during growth. Initially, the growth is slow because of the absence of growth nuclei and rapid re-evaporation of the material into vacuum. As the growth proceeds, more stable island perimeter becomes available and it speeds up, just to get slower again, when the first layer is about to complete and the available island perimeter to attach to becomes smaller. This is visible as the first inflection on the hue curve. The growth


DOI: 10.1021/acsami.8b10857
ACS Appl. Mater. Interfaces 2018, 10, 33457−33463

stopped at this point shows a single-layer Raman signal, as shown in the inset on the right.

If the growth process is continued at the unchanged filament temperature, substrate temperature, and $CS_2$ gas concentration, then the second layer nucleates, increases in size, speeds up in growth, and the growth decelerates again once it nears completion. By stopping the growth at this point, a bilayer film is produced with the corresponding Raman signal (inset). If the film growth is continued, the trilayer color (inset) is reached and ultimately a thick film emerges.

In order to achieve the highest quality films, the actual growth process proceeds not at constant filament brightness as used in the experiment of Figure 2. Rather as each layer nears completion, the filament temperature is reduced gradually to slow down the growth and allow optimal ripening/arrangement of the interisland/domain boundaries as well as evaporation of any adlayer islands that may have formed during the growth process. The Supporting Information (Figure S6) shows a scanning transmission electron microscopy (STEM) image that corroborates attachment between adjacent grain boundaries, which is important for film utility. If another layer is desired, the filament temperature is increased again to speed up the film growth and reduced again toward the completion of the next layer.

The Raman spectra in the inset of Figure 2 show the $E^1_{2g}$ in-plane and $A_{1g}$ out-of-plane peaks for different layer thicknesses. The peak separations are 19 (1L), 22 (2L), 23 (3L), and 25 (bulk) $cm^{-1}$. The separations match well the literature values for mono-, bi-, trilayer and bulk $MoS_2$.[6,7]

Mapping of the Raman $E^1_{2g}$ and $A_{1g}$ peak separation confirms the homogeneity of the material. Figure 3a–c shows

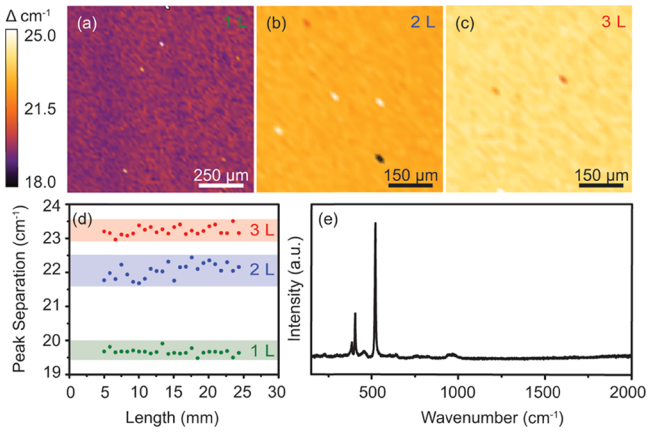


**Figure 3.** (a–c) Spatial mapping of the separation of the in-plane ($E^1_{2g}$) and out-of-plane ($A_{1g}$) modes of single-, bi-, and trilayer films, respectively. The values of 19.5, 22, and 23 $cm^{-1}$ are tell-tale of the respective film thickness. (d) Trace of the Raman peak separation in steps of 840 $\mu$m across 1 in. of a wafer substrate. (e) Extended range of the Raman spectrum for the single-layer $MoS_2$ film.

millimeter-scale maps of the peak separation; at each layer thickness, the variation is well below one wavenumber. The isolated white and black dots are caused by the dust deposited onto the sample during Raman mapping in ambient unfiltered air and are not a consequence of the growth process. In order to ascertain the homogeneity of the film over a large range, we took Raman spectra at 840 $\mu$m separation across a wafer refocusing the beam at each location. Figure 3d shows the results and affirms the large range homogeneity of the wafer beyond the millimeter-scale map areas of Figure 3a–c.

Despite the use of carbon disulfide as a precursor, we find no Raman signature of a carbon film (Figure 3e). The presence of strong photoluminescence (PL) (as strong as on exfoliated samples) is a further indicator of the absence of a carbon film. X-ray photoelectron spectroscopy measurements of the substrate before and after transfer of an $MoS_2$ film show no significant difference of carbon trace contamination.

The PL is an indicator of the film quality and sensitive to adsorbed contaminants, strain, and other extrinsic effects. A typical PL spectrum of the film is shown in Figure 4a. The A exciton is found at 1.89–1.90 eV, slightly blue-shifted compared to conventional CVD and exfoliated materials.[36] We attribute this to strain induced by the higher thermal expansion coefficient of the $SiO_2$ substrate as compared to the $MoS_2$ film, leading to compressive strain during cooling down from growth temperatures, as is to be expected for a continuous film. Compressive strain of $MoS_2$ is typically associated with a blue shift of the PL signature, as observed here.[37] Occasionally, we find across the wafer (on the millimeter scale) strain relief patterns manifested as a slight shift (<0.03 eV) of the PL peak position (Figure S3). This finding ascertains the mechanical continuity of our film at the wafer scale. The full width at half-maximum of the PL peak is consistently at an excellent value of ∼0.077 eV. The PL brightness of the films rivals the best exfoliated and CVD samples we have produced. The B exciton is barely visible at 2.06 eV, further confirming the material quality. Mapping of the PL peak position across the sample shows variations on the single-digit millielectronvolt (meV) scale only (Figure 4b).

SEM images of the $MoS_2$ single-layer film are featureless at any length scale (Figure S5). The atomic force microscopy root-mean-square surface roughness is at 0.2 Å slightly better than that of the bare $SiO_2$ substrate before the growth. Transfer of the film onto a grid for STEM reveals a highly ordered array of $MoS_2$ unit cells at the expected periodicity (3.31 Å) of the 2H phase (Figure 4c). Extended areas of single-crystalline domains are surrounded by a band of a number of very small (∼10 nm) domains, validating the growth mode described above. The Supporting Information (Figure S6) shows that adjacent extended domains are chemically connected through the small domain band surrounding them, as is important for transport applications.

Appealing transport properties of the film are crucial for the technological application of the method. Electron beam lithography was used to fabricate 50 FET test structures using the oxide of the growth substrate as the gate dielectric (bottom-gated without transfer). It is important to highlight that our growth process is sufficiently benign to the substrate that oxide pinholes resulting in gate leakage are absent. We use a device geometry that includes the channel length/width of 0.25/20 $\mu$m (see insets in Figure 5a for the optical image of the device). The electrodes were fabricated from a stack of 5 nm of yttrium for adhesion and 50 nm of gold. At source–drain voltage $V_{sd}$ below 0.5 V, the output current voltage characteristics (source–drain current $I_{sd}$ as a function of the source–drain voltage $V_{sd}$) were linear and symmetric, indicating near-Ohmic properties of the drain and source contacts. Figure 5a shows the measured output characteristics at high drain voltage up to 4 V. This biasing condition corresponds to the 160 kV/cm electric field in the channel and power density dissipated by the channel of the order of $10^9$ W/


DOI: 10.1021/acsami.8b10857
ACS Appl. Mater. Interfaces 2018, 10, 33457–33463

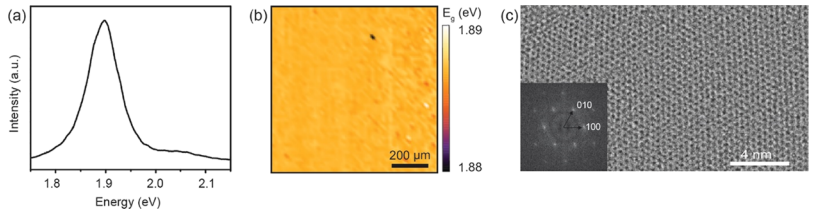


**Figure 4.** (a) PL spectrum of a single-layer $MoS_2$ film. (b) Mapping of the A-exciton position across 1 × 1 millimeter of the sample area reveals variations well below 10 meV (full color scale). (c) STEM image of the crystalline structure of the film. The inset shows the Fourier transformation and two indexed peaks.

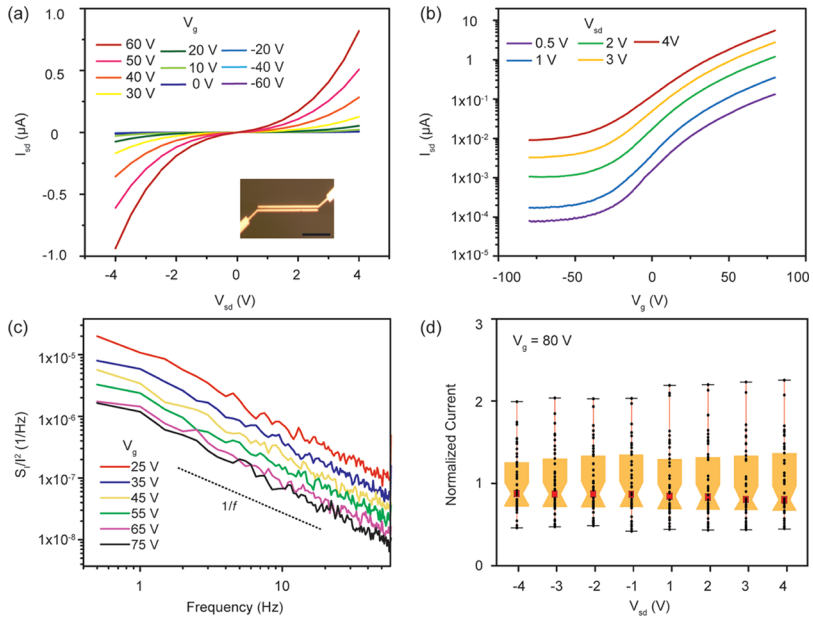


**Figure 5.** (a) $I-V$ characteristics of the single-layer $MoS_2$ film at different gate voltages. Inset of an optical image of the device structure. The scale bar is 10 $\mu$m. (b) Source−drain current as a function of gate voltage for a single-layer $MoS_2$ device. (c) Noise power as a function of frequency. (d) Box and whisker plots of the variation of $I_{sd}$ at fixed $V_g$ and for a set of $V_{sd}$, normalized to the average $I_{sd}$ at the respective $V_{sd}$. Data are collected from 47 devices evenly spread across >1 $cm^2$ of the substrate area.

$cm^3$. The reliable operation of mass-fabricated devices at these extreme conditions indicates the high quality of the material. It is known that the temperature dependence of the current voltage characteristics in this type of $MoS_2$ transistors is governed by two competing mechanisms: decrease of the threshold voltage and decrease of the mobility with the temperature increase.[10] The superlinearity of the characteristics in Figure 4a can be naturally explained by the Joule heating, causing a decrease of the threshold voltage and a small degradation of the mobility.

Figure 5b shows the measured current as a function of applied gate voltage at fixed source−drain biases. The characteristics in Figure 5b do not show any trend of saturation at high gate voltage and are quite typical for bottom-gated $MoS_2$ devices in the absence of engineered contacts, such as edge contacts or the use of graphene as a contact material. The low apparent mobility in these devices on the order of 1 can directly be attributed to the common challenge of contacts to $MoS_2$ devices rather than indicating a property of the film; we expect that integration of top-/dual gating and engineered contacts would show the full potential of this material.[38−45]

The level of the low-frequency noise is an important metric of the material quality and suitability for electronic applications.[46] It is particularly important for 2D materials where conduction electrons in the device channel are ultimately exposed to various defects in the gate dielectric and top surface.[47] The level of the low-frequency noise can be used to assess the concentration of defects and material tolerance to electromigration. In practical applications, the low-frequency noise defines the phase noise in communication systems and sets the limits for sensor sensitivity and selectivity. The low-frequency noise was measured in the frequency range of 1−50 Hz at room temperature. The devices were biased in a common source mode. Details of our noise measurement procedures have been reported by some of us elsewhere.[48−50] Figure 4c shows the normalized noise spectral density $S_I/I_{ds}^2$ as a function of frequency for a representative $MoS_2$ device. The noise is of clear $1/f$ type ($f$ is a frequency). The absence of the generation—recombination bulges indicates that there are no high concentrations of any specific defect, which would dominate the low-frequency noise response. The noise spectral density reveals scaling with the applied gate bias, that is, carrier concentration in the channel, expected for semiconductor devices.[51] The $1/f$ noise level in FETs is often characterized by the noise amplitude normalized to the channel area.[52] The minimum noise level measured in studied devices was of the order $2 \times 10^{-7}$ $Hz^{-1}$ $\mu m^2$. This is smaller than that reported in earlier publications for $MoS_2$ transistors implemented with the exfoliated or CVD material.[49,53] The latter provides an


DOI: 10.1021/acsami.8b10857
ACS Appl. Mater. Interfaces 2018, 10, 33457−33463

additional confirmation of the material quality from the device applications' point of view.

In order to demonstrate the homogeneity of the film, we fabricated a set of 50 devices evenly spaced across more than 1 $cm^2$ of the substrate area. Of the 50 devices fabricated, one had a failure of the electron beam during writing and two were lithographically nonviable. Figure 5d shows a box and whisker plot of the variation of $I_{sd}$ at different $V_{sd}$ across all remaining 47 devices. We find a maximum variation by a factor of 2 and an interquartile range of 0.8−1.3 with 1 normalized to the average current at any $V_{sd}$.

## CONCLUSIONS

In conclusion, the scalable growth of continuous single- and few-layer $MoS_2$ is demonstrated using a high-vacuum deposition process. Optical and electrical characterizations validate high quality and homogeneity of the material as well as superior noise performance. We highlight that these results are achieved using an amorphous $SiO_2$ substrate and without any powder or metal−organic precursors. Using the color of light reflected from the substrate, process control at the single-layer limit is achieved.

## METHODS

**High-Vacuum Growth.** The $MoS_2$ growth reactor is an ultrahigh-vacuum system equipped with a turbo pump, ion gauge, and so forth for facile preparation of high vacuum. It houses a 3 in. hot-plate style heater (MeiVac) and a leak valve for the introduction of $CS_2$ based on its native vapor pressure. We typically use silicon wafers with 300 nm dry oxide $SiO_2$ (WaferPro). While at a base pressure of $1 \times 10^{-7}$ Torr, the sample is heated to 650 °C. The $CS_2$ leak valve is opened to increase the chamber pressure to $6 \times 10^{-4}$ Torr. Six separate molybdenum wires, each 4 in. long with a diameter of 0.5 mm and a separation of 1 in., provide the molybdenum source. The molybdenum filaments are resistively heated until they are approximately 1800 °C for up to 60 min, while the total filament power is controlled. The growth is monitored by colorimetric measurements using a standard microscope camera (OMAX). Using thresholding of the brightness, the reflection from the filaments is identified and the local average hue value is calculated. During the initial 10 min of the growth period, the filament power is pushed to reach the maximum filament temperature of 1800 °C for quick nucleation; as the single layer nears completion, the filament power is dropped and held steady to complete each layer before the next is nucleated. Subsequent layers can be formed by repeating the same process. After the filaments are switched off, the substrate heater is allowed to cool naturally. Once it reaches 200 °C, the $CS_2$ flow is stopped, the chamber is vented with nitrogen, and the wafer is removed.

**Optical Characterization.** The samples were analyzed with Raman and PL spectroscopy using a HORIBA LabRAM instrument with a 532 nm excitation laser. The Raman and PL measurements used 1800 and 600 gratings, respectively.

**Device Fabrication.** After the material is grown, C5 PMMA is spin-coated onto the sample at 4000 rpm for 45 s and is then baked at 180 °C for a ∼600 nm thick layer of resist. The electrodes and pads are patterned onto the sample using electron beam lithography. Immediately after patterning, the sample is developed in 1:3 MIBK to IPA and IPA for 10 and 20 s, respectively. After the pattern is developed, the electrode material is deposited using electron beam evaporation of Y/Au (5 nm/50 nm). The sample is placed into acetone for 20 min to lift off the residual metal.

**Electron Microscopy.** $MoS_2$ for the SEM image was grown on a bare silicon substrate that was cleaned using a buffer oxide etch solution. Imaging proceeded in FEI XL30-FEG SEM. The TEM samples were prepared by using KOH solution to transfer the film to a TEM grid. The samples were analyzed using FEI Titan Themis 300. The fast Fourier transform (FFT) of the material was obtained using the ImageJ FFT analysis of the TEM image provided.

## ASSOCIATED CONTENT

### Supporting Information

The Supporting Information is available free of charge on the ACS Publications website at DOI: 10.1021/acsami.8b10857.

Photograph of the growth chamber and further optical, spectroscopic, and electron microscopy characterization of the films (PDF)

## AUTHOR INFORMATION


### Corresponding Author

*E-mail: bartels@ucr.edu.

### ORCID

Ludwig Bartels: 0000-0002-3964-4538

### Present Address

†Ioffe Physical-Technical Institute, St. Petersburg 194021 Russia.


### Notes

The authors declare no competing financial interest.

## ACKNOWLEDGMENTS

This work was supported, in part, by the Semiconductor Research Corporation (SRC) contract 2018-NM-2796: One-Dimensional Single-Crystal vdW Metals: Ultimately Down-scaled Interconnects with Exceptional Current-Carrying Capacity and Reliability. The work in the Bartels group was also supported by the US Air Force Office of Scientific Research grant FA9550-17-1-0377. The work in the Balandin Group was also supported by the National Science Foundation (NSF) through the Emerging Frontiers of Research Initiative (EFRI) 2-DARE award EFRI-1433395: Novel Switching Phenomena in Atomic $MX_2$ Heterostructures for Multifunctional Applications and UC—National Laboratory Collaborative Research and Training Program UCRI CRT: LFR-17-477237: Mesoscopic 2D Materials: Many-Body Interactions and Applications. K.A., M.W., and A.J.B. thank the US National Science Foundation for Research Experience for Undergraduate Students Fellowship Support through DMR 1659450.

## REFERENCES

(1) Butler, S. Z.; Hollen, S. M.; Cao, L.; Cui, Y.; Gupta, J. A.; Gutiérrez, H. R.; Heinz, T. F.; Hong, S. S.; Huang, J.; Ismach, A. F.; Johnston-Halperin, E.; Kuno, M.; Plashnitsa, V. V.; Robinson, R. D.; Ruoff, R. S.; Salahuddin, S.; Shan, J.; Shi, L.; Spencer, M. G.; Terrones, M.; Windl, W.; Goldberger, J. E. Progress, Challenges, and Opportunities in Two-Dimensional Materials Beyond Graphene. *ACS Nano* **2013**, *7*, 2898−2926.

(2) Choi, W.; Choudhary, N.; Han, G. H.; Park, J.; Akinwande, D.; Lee, Y. H. Recent Development of Two-Dimensional Transition Metal Dichalcogenides and Their Applications. *Mater. Today* **2017**, *20*, 116−130.

(3) Bhimanapati, G. R.; Lin, Z.; Meunier, V.; Jung, Y.; Cha, J.; Das, S.; Xiao, D.; Son, Y.; Strano, M. S.; Cooper, V. R.; Liang, L.; Louie, S. G.; Ringe, E.; Zhou, W.; Kim, S. S.; Naik, R. R.; Sumpter, B. G.; Terrones, H.; Xia, F.; Wang, Y.; Zhu, J.; Akinwande, D.; Alem, N.; Schuller, J. A.; Schaak, R. E.; Terrones, M.; Robinson, J. A. Recent Advances in Two-Dimensional Materials Beyond Graphene. *ACS Nano* **2015**, *9*, 11509−11539.

(4) Özçelik, V. O.; Azadani, J. G.; Yang, C.; Koester, S. J.; Low, T. Band Alignment of Two-Dimensional Semiconductors for Designing



DOI: 10.1021/acsami.8b10857
ACS Appl. Mater. Interfaces 2018, 10, 33457−33463

Heterostructures with Momentum Space Matching. *Phys. Rev. B* **2016**, *94*, 035125.
(5) Sarkar, D.; Xie, X.; Liu, W.; Cao, W.; Kang, J.; Gong, Y.; Kraemer, S.; Ajayan, P. M.; Banerjee, K. A Subthermionic Tunnel Field-Effect Transistor with an Atomically Thin Channel. *Nature* **2015**, *526*, 91−95.
(6) Mak, K. F.; Lee, C.; Hone, J.; Shan, J.; Heinz, T. F. Atomically Thin $MoS_2$: A New Direct-Gap Semiconductor. *Phys. Rev. Lett.* **2010**, *105*, 136805.
(7) Splendiani, A.; Sun, L.; Zhang, Y.; Li, T.; Kim, J.; Chim, C.-Y.; Galli, G.; Wang, F. Emerging Photoluminescence in Monolayer MoS2. *Nano Lett.* **2010**, *10*, 1271−1275.
(8) Mak, K. F.; He, K.; Shan, J.; Heinz, T. F. Control of valley polarization in monolayer MoS2 by optical helicity. *Nat. Nanotechnol.* **2012**, *7*, 494−498.
(9) Cao, T.; Wang, G.; Han, W.; Ye, H.; Zhu, C.; Shi, J.; Niu, Q.; Tan, P.; Wang, E.; Liu, B.; Feng, J. Valley-Selective Circular Dichroism of Monolayer Molybdenum Disulphide. *Nat. Commun.* **2012**, *3*, 887.
(10) Jiang, C.; Rumyantsev, S. L.; Samnakay, R.; Shur, M. S.; Balandin, A. A. High-temperature performance of MoS2 thin-film transistors: Direct current and pulse current-voltage characteristics. *J. Appl. Phys.* **2015**, *117*, 064301.
(11) Samnakay, R.; Jiang, C.; Rumyantsev, S. L.; Shur, M. S.; Balandin, A. A. Selective chemical vapor sensing with few-layer MoS2 thin-film transistors: Comparison with graphene devices. *Appl. Phys. Lett.* **2015**, *106*, 023115.
(12) Liu, G.; Rumyantsev, S. L.; Jiang, C.; Shur, M. S.; Balandin, A. A. Selective Gas Sensing With $h$ -BN Capped MoS2 Heterostructure Thin-Film Transistors. *IEEE Electron. Device Lett.* **2015**, *36*, 1202−1204.
(13) Lee, Y.-H.; Zhang, X.-Q.; Zhang, W.; Chang, M.-T.; Lin, C.-T.; Chang, K.-D.; Yu, Y.-C.; Wang, J. T.-W.; Chang, C.-S.; Li, L.-J.; Lin, T.-W. Synthesis of Large-Area MoS2Atomic Layers with Chemical Vapor Deposition. *Adv. Mater.* **2012**, *24*, 2320−2325.
(14) Mann, J.; Sun, D.; Ma, Q.; Chen, J.-R.; Preciado, E.; Ohta, T.; Diaconescu, B.; Yamaguchi, K.; Tran, T.; Wurch, M.; Magnone, K.; Heinz, T. F.; Kellogg, G. L.; Kawakami, R.; Bartels, L. Facile Growth of Sub-Millimeter Scale Monolayer $MoS_2$ Films on $SiO_2$/Si. *Eur. Phys. J. B* **2013**, *86*, 226.
(15) Najmaei, S.; Liu, Z.; Zhou, W.; Zou, X.; Shi, G.; Lei, S.; Yakobson, B. I.; Idrobo, J.-C.; Ajayan, P. M.; Lou, J. Vapour Phase Growth and Grain Boundary Structure of Molybdenum Disulphide Atomic Layers. *Nat. Mater.* **2013**, *12*, 754−759.
(16) Ling, X.; Lee, Y.-H.; Lin, Y.; Fang, W.; Yu, L.; Dresselhaus, M. S.; Kong, J. Role of the Seeding Promoter in MoS2 Growth by Chemical Vapor Deposition. *Nano Lett.* **2014**, *14*, 464−472.
(17) Shaw, J. C.; Zhou, H.; Chen, Y.; Weiss, N. O.; Liu, Y.; Huang, Y.; Duan, X. Chemical vapor deposition growth of monolayer MoSe2 nanosheets. *Nano Res.* **2014**, *7*, 511−517.
(18) Tongay, S.; Fan, W.; Kang, J.; Park, J.; Koldemir, U.; Suh, J.; Narang, D. S.; Liu, K.; Ji, J.; Li, J.; Sinclair, R.; Wu, J. Tuning Interlayer Coupling in Large-Area Heterostructures with CVD-Grown MoS2 and WS2 Monolayers. *Nano Lett.* **2014**, *14*, 3185−3190.
(19) Dumcenco, D.; Ovchinnikov, D.; Marinov, K.; Lazić, P.; Gibertini, M.; Marzari, N.; Sanchez, O. L.; Kung, Y.-C.; Krasnozhon, D.; Chen, M.-W.; Bertolazzi, S.; Gillet, P.; Morral, A. F. i.; Radenovic, A.; Kis, A. Large-Area Epitaxial Monolayer MoS2. *ACS Nano* **2015**, *9*, 4611−4620.
(20) Velusamy, D. B.; Kim, R. H.; Cha, S.; Huh, J.; Khazaeinezhad, R.; Kassani, S. H.; Song, G.; Cho, S. M.; Cho, S. H.; Hwang, I.; Lee, J.; Oh, K.; Choi, H.; Park, C. Flexible Transition Metal Dichalcogenide Nanosheets for Band-Selective Photodetection. *Nat. Commun.* **2015**, *6*, 8063.
(21) Kappera, R.; Voiry, D.; Yalcin, S. E.; Branch, B.; Gupta, G.; Mohite, A. D.; Chhowalla, M. Phase-engineered low-resistance contacts for ultrathin MoS2 transistors. *Nat. Mater.* **2014**, *13*, 1128−1134.
(22) Kang, J.; Seo, J.-W. T.; Alducin, D.; Ponce, A.; Yacaman, M. J.; Hersam, M. C. Thickness Sorting of Two-Dimensional Transition Metal Dichalcogenides Via Copolymer-Assisted Density Gradient Ultracentrifugation. *Nat. Commun.* **2014**, *5*, 5478.
(23) Kang, K.; Xie, S.; Huang, L.; Han, Y.; Huang, P. Y.; Mak, K. F.; Kim, C.-J.; Muller, D.; Park, J. High-Mobility Three-Atom-Thick Semiconducting Films with Wafer-Scale Homogeneity. *Nature* **2015**, *520*, 656−660.
(24) Shinde, S. M.; Das, T.; Hoang, A. T.; Sharma, B. K.; Chen, X.; Ahn, J.-H. Surface-Functionalization-Mediated Direct Transfer of Molybdenum Disulfide for Large-Area Flexible Devices. *Adv. Funct. Mater.* **2018**, *28*, 1706231.
(25) Kalanyan, B.; Kimes, W. A.; Beams, R.; Stranick, S. J.; Garratt, E.; Kalish, I.; Davydov, A. V.; Kanjolia, R. K.; Maslar, J. E. Rapid Wafer-Scale Growth of Polycrystalline 2H-MoS2 by Pulsed Metal-Organic Chemical Vapor Deposition. *Chem. Mater.* **2017**, *29*, 6279−6288.
(26) Ho, T. A.; Bae, C.; Lee, S.; Kim, M.; Montero-Moreno, J. M.; Park, J. H.; Shin, H. Edge-On MoS2 Thin Films by Atomic Layer Deposition for Understanding the Interplay between the Active Area and Hydrogen Evolution Reaction. *Chem. Mater.* **2017**, *29*, 7604−7614.
(27) Tan, L. K.; Liu, B.; Teng, J. H.; Guo, S.; Low, H. Y.; Loh, K. P. Correction: Atomic layer deposition of a MoS2film. *Nanoscale* **2014**, *6*, 14002.
(28) Mattinen, M.; Hatanpää, T.; Sarnet, T.; Mizohata, K.; Meinander, K.; King, P. J.; Khriachtchev, L.; Räisänen, J.; Ritala, M.; Leskelä, M. Atomic Layer Deposition of Crystalline MoS2 Thin Films: New Molybdenum Precursor for Low-Temperature Film Growth. *Adv. Mater. Interfaces* **2017**, *4*, 1700123.
(29) Pyeon, J. J.; Kim, S. H.; Jeong, D. S.; Baek, S.-H.; Kang, C.-Y.; Kim, J.-S.; Kim, S. K. Wafer-scale growth of MoS2thin films by atomic layer deposition. *Nanoscale* **2016**, *8*, 10792−10798.
(30) Jang, Y.; Yeo, S.; Lee, H.-B.-R.; Kim, H.; Kim, S.-H. Wafer-scale, conformal and direct growth of MoS 2 thin films by atomic layer deposition. *Appl. Surf. Sci.* **2016**, *365*, 160−165.
(31) Zhou, D.; Shu, H.; Hu, C.; Jiang, L.; Liang, P.; Chen, X. Unveiling the Growth Mechanism of MoS2 with Chemical Vapor Deposition: From Two-Dimensional Planar Nucleation to Self-Seeding Nucleation. *Cryst. Growth Des.* **2018**, *18*, 1012−1019.
(32) Zhu, D.; Shu, H.; Jiang, F.; Lv, D.; Asokan, V.; Omar, O.; Yuan, J.; Zhang, Z.; Jin, C. Capture the Growth Kinetics of CVD Growth of Two dimensional $MoS_2$. *Npj 2d Mater. Appl.* **2017**, *1*, 1−8.
(33) Ji, Q.; Zhang, Y.; Zhang, Y.; Liu, Z. Chemical Vapour Deposition of Group-VIB Metal Dichalcogenide Monolayers: Engineered Substrates from Amorphous to Single Crystalline. *Chem. Soc. Rev.* **2015**, *44*, 2587−2602.
(34) Blake, P.; Hill, E. W.; Castro Neto, A. H.; Novoselov, K. S.; Jiang, D.; Yang, R.; Booth, T. J.; Geim, A. K. Making Graphene Visible. *Appl. Phys. Lett.* **2007**, *91*, 063124.
(35) Zhang, H.; Wan, Y.; Ma, Y.; Wang, W.; Wang, Y.; Dai, L. Interference Effect on Optical Signals of Monolayer $MoS_2$. *Appl. Phys. Lett.* **2015**, *107*, 101904.
(36) Plechinger, G.; Mann, J.; Preciado, E.; Barroso, D.; Nguyen, A.; Eroms, J.; Schüller, C.; Bartels, L.; Korn, T. A direct comparison of CVD-grown and exfoliated MoS2using optical spectroscopy. *Semicond. Sci. Technol.* **2014**, *29*, 064008.
(37) Johari, P.; Shenoy, V. B. Tunable Dielectric Properties of Transition Metal Dichalcogenides. *ACS Nano* **2011**, *5*, 5903−5908.
(38) Singh, A. K.; Hwang, C.; Eom, J. Low-Voltage and High-Performance Multilayer MoS2 Field-Effect Transistors with Graphene Electrodes. *ACS Appl. Mater. Interfaces* **2016**, *8*, 34699−34705.
(39) Zhao, M.; Ye, Y.; Han, Y.; Xia, Y.; Zhu, H.; Wang, S.; Wang, Y.; Muller, D. A.; Zhang, X. Large-Scale Chemical Assembly of Atomically Thin Transistors and Circuits. *Nat. Nanotechnol.* **2016**, *11*, 954−959.
(40) Baik, S. S.; Im, S.; Choi, H. J. Work Function Tuning in Two-Dimensional $MoS_2$ Field-Effect-Transistors with Graphene and Titanium Source-Drain Contacts. *Sci. Rep.* **2017**, *7*, 45546.


DOI: 10.1021/acsami.8b10857
*ACS Appl. Mater. Interfaces* 2018, 10, 33457−33463

(41) Andleeb, S.; Eom, J.; Naz, N. R.; Singh, A. K. MoS2 field-effect transistor with graphene contacts. *J. Mater. Chem. C* **2017**, *5*, 8308−8314.
(42) Radisavljevic, B.; Radenovic, A.; Brivio, J.; Giacometti, V.; Kis, A. Single-layer MoS2 transistors. *Nat. Nanotechnol.* **2011**, *6*, 147−150.
(43) Radisavljevic, B.; Kis, A. Reply to 'Measurement of mobility in dual-gated MoS2 transistors'. *Nat. Nanotechnol.* **2013**, *8*, 147−148.
(44) Fuhrer, M. S.; Hone, J. Measurement of mobility in dual-gated MoS2 transistors. *Nat. Nanotechnol.* **2013**, *8*, 146−147.
(45) Liu, H.; Ye, P. D. $\hbox{MoS}_{2}$ Dual-Gate MOSFET With Atomic-Layer-Deposited $\hbox{Al}_{2}\hbox{O}_{3}$ as Top-Gate Dielectric. *IEEE Electron. Device Lett.* **2012**, *33*, 546−548.
(46) Balandin, A. A. *Noise and Fluctuations Control in Electronic Devices*; American Scientific Publishers: Stevenson Ranch, CA, 2002.
(47) Balandin, A. A. Low-Frequency 1/f Noise in Graphene Devices. *Nat. Nanotechnol.* **2013**, *8*, 549−555.
(48) Renteria, J.; Samnakay, R.; Rumyantsev, S. L.; Jiang, C.; Goli, P.; Shur, M. S.; Balandin, A. A. Low-frequency 1/f noise in MoS2 transistors: Relative contributions of the channel and contacts. *Appl. Phys. Lett.* **2014**, *104*, 153104.
(49) Rumyantsev, S. L.; Jiang, C. L.; Samnakay, R.; Shur, M. S.; Balandin, A. A. 1/f Noise Characteristics of $MoS_2$ Thin-Film Transistors: Comparison of Single and Multilayer Structures. *IEEE Electron. Device Lett.* **2015**, *36*, 517−519.
(50) Liu, G.; Rumyantsev, S.; Bloodgood, M. A.; Salguero, T. T.; Shur, M.; Balandin, A. A. Low-Frequency Electronic Noise in Quasi-1D TaSe3 van der Waals Nanowires. *Nano Lett.* **2017**, *17*, 377−383.
(51) Dmitriev, A. P.; Levinshtein, M. E.; Rumyantsev, S. L. On the Hooge Relation in Semiconductors and Metals. *J. Appl. Phys.* **2009**, *106*, 024514.
(52) Rumyantsev, S.; Liu, G.; Stillman, W.; Shur, M.; Balandin, A. A. Electrical and Noise Characteristics of Graphene Field-Effect Transistors: Ambient Effects, Noise Sources and Physical Mechanisms. *J. Phys. Condens. Matter* **2010**, *22*, 395302.
(53) Wang, J.-W.; Liu, Y.-P.; Chen, P.-H.; Chuang, M.-H.; Pezeshki, A.; Ling, D.-C.; Chen, J.-C.; Chen, Y.-F.; Lee, Y.-H. Controlled Low-Frequency Electrical Noise of Monolayer MoS2 with Ohmic Contact and Tunable Carrier Concentration. *Adv. Electron. Mater.* **2018**, *4*, 1700340.


DOI: 10.1021/acsami.8b10857
*ACS Appl. Mater. Interfaces* 2018, 10, 33457−33463